ACS OMEGA

http://pubs.acs.org/journal/acsodf

Article

Adsorption and Sensing of SF_6 Decomposition Products by a Pd-Doped $MoTe_2$ Monolayer: A First-Principles Study

Chengjun Li, Zengting Wang, Shuangshuang Tian,* and Ying Zhang

Cite This: *ACS Omega* 2023, 8, 28769−28777

Read Online

ACCESS | Metrics & More | Article Recommendations

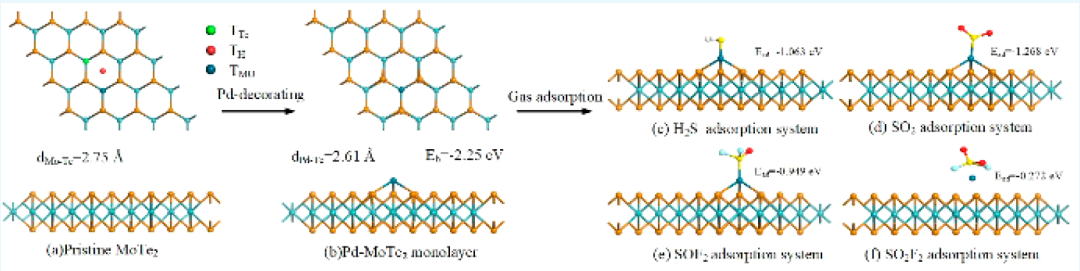

ABSTRACT: The detection of sulfur hexafluoride (SF_6) decomposition components has become one of the best ways to diagnose early latent insulation faults in gas-insulated equipment, which can effectively prevent sudden accidents by identifying such faults. In this paper, we by first-principles theory investigated the adsorption and sensing behaviors of four typical SF_6 decomposition components (H_2S, SO_2, SOF_2, and SO_2F_2) on the pristine Pd-doped $MoTe_2$ monolayer. The adsorption energy, work function, recovery time, charge density difference, density of state, and band structure of the adsorption structures are obtained as well as analyzed. The results indicate that the Pd dopant prefers to be trapped at the T_{Mo} site, with a binding energy of −2.25 eV. The Pd-$MoTe_2$ chemisorbs the remaining gases except SO_2xF_2, with the adsorption capacity ranking as SOF_2 > SO_2 > H_2S. The adsorption of gas molecules reduces the bandgap of Pd-$MoTe_2$, thereby increasing conductivity. On the other hand, the recovery time of the Pd-$MoTe_2$ monolayer material at a temperature of 398 K demonstrates its excellent gas desorption performance toward four decomposition gases. The research results provide a theoretical basis for Pd-$MoTe_2$ to detect SF_6 decomposition components, thus, promoting the stable operation of the power system.

1. INTRODUCTION

Due to its excellent insulation and arc extinguishing properties, SF_6 is widely used in high-voltage equipment and gas insulation systems.[1−3] However, during long-term operation, SF_6 will inevitably decompose into a series of low-fluoride sulfides due to partial discharge caused by unavoidable insulation defects within the equipment. These byproducts react quickly with micro-oxygen and microwater in the gas insulation system, generating a series of relatively stable chemical components, including SO_2, SOF_2, H_2S, SO_2F_2, HF, etc.[4−6] If not properly handled, they not only pose a risk to human health but also corrode the insulation system, exacerbate discharges, and affect the stability of system operation.[7] Therefore, taking effective measures to inspect these gases and ensure the insulation status of electrical equipment is necessary.[8−11]

The gas sensing capabilities of transition-metal dichalcogenides (TMDs) have garnered considerable attention[12−15] due to their superior gas adsorption carrier mobility and large surface-to-volume ratio, which is extensively considered to have strong sensing potential.[16−18] $MoTe_2$, a representative TMD with semiconductive, semimetallic properties and a lower bandgap, has been extensively studied and applied recently.[19,20] Wang et al.[21] investigated the adsorption of toxic CO gas on TM (Ni, Pd, Pt)-doped $MoTe_2$ monolayer and discovered that transition metal doping enhances the conductivity of $MoTe_2$, thereby improving its sensitivity toward CO gas detection. Zhu et al.[22] studied the adsorption of Rh on SF_6 and found the adsorption behavior of the Rh-$MoTe_2$ monolayer on three gases followed the order SO_2F_2 > SO_2 > SOF_2. This outcome suggests that Rh-$MoTe_2$ is an excellent absorbent for removing SO_2F_2 from SF_6 insulated equipment. Pd, celebrated for its exceptional catalytic performance and chemical stability, is frequently used as a doping atom for a range of materials. Nonetheless, research on Pd-doped $MoTe_2$ (Pd-$MoTe_2$) predominantly focuses on detecting

Received: May 22, 2023
Accepted: July 10, 2023
Published: July 25, 2023

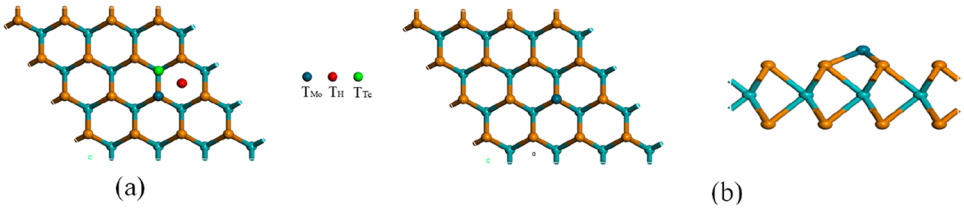

Figure 1. MSC of (a) pristine and (b) Pd-$MoTe_2$ monolayers.

common gases such as NH_3, SO_2, and NO_2,[21,23] and with no applications yet in detecting SF_6 decomposition components.

In this work, we focus on using a Pd-$MoTe_2$ monolayer as a sensing material to target four typical SF_6 decomposition components for adsorption: SO_2, SO_2F_2, SOF_2, and H_2S. Based on the first-principles of density functional theory (DFT),[24] this paper thoroughly investigates and assesses their surface interactions at the microscopic level. The findings from this study establish a theoretical basis for the preparation of Pd-$MoTe_2$ gas-sensitive materials and the development of high-performance gas sensors for SF_6 decomposition component detection.

2. COMPUTATIONAL DETAILS

We employ the DMol[3] module in the Materials Studio (MS) to perform geometry optimization on the Pd-$MoTe_2$ monolayer, thereby ensuring the model structure's stability. First, a 4*4*1 $MoTe_2$ monolayer supercell is established, which contains 16 Mo atoms and 32 Te atoms.[25] To prevent interaction between adjacent layers, we set the thickness of the vacuum layer to 20 Å. For computational purposes, we utilize the Perdew−Burke−Ernzerhof (PBE) functional within the generalized gradient approximation (GGA) method for addressing the exchange-correlation functional between electrons. The DFT-D method, which was customized by TS, was used to understand the van der Waals force and long-range interactions.[26] Concurrently, double numerical polarization (DNP) is used as the basis function of the linear combination of the atomic orbitals method. DFT Semicore pseudopotential (DSPP)[27] is used to handle transition metals. For static electronic structure calculations, the self-consistent loop energy of 10^{-6} Ha, global orbital cutoff radius of 5.0 Å, and smearing of 0.005 Ha are determined to ensure the accuracy of the total energy. The energy tolerance accuracy, maximum force, and displacement were selected as 10^{-5} Ha, 2 × 10^{-3} Ha/Å, and 5 × 10^{-3} Å, respectively.[28] In all charge density and energy calculations, the Monkhorst−Pack k-point is set to 3 × 3 × 1 to improve the accuracy of the calculation.

3. RESULTS AND DISCUSSION

3.1. Analysis of the Pd-$MoTe_2$ Monolayer. To shorten the paragraph, we only plot and analyze the most stable configurations (MSC) for the Pd-$MoTe_2$ monolayer and gas adsorption configurations. As plotted in Figure 1, the possible adsorption sites are shown in Figure 1a. It is seen in Figure 1a that three sites are considered, including T_H, T_{Mo}, and T_{Te}. T_H is the location above the center of the $MoTe_2$ hexagonal ring, T_{Mo} is the location on the top of the Mo atom, and T_{Te} is the location on the top of the Te atom. The binding energy (E_b) of the Pd atom on the $MoTe_2$ monolayer is defined in Equation 1, where $E_{Pd\text{-}MoTe_2}$, E_{Pd}, and E_{MoTe_2} represent the energy of Pd-$MoTe_2$ monolayer, Pd atom, and pristine $MoTe_2$ monolayer, respectively.

$$E_{binding} = E_{Pd\text{-}MoTe_2} - E_{Pd} - E_{MoTe_2} \quad (1)$$

Table 1 indicates that the most stable structure is achieved by doping the Pd atom on top of the Mo atom, with a binding energy of −2.25 eV. Consequently, the adsorption of the four gases discussed in this study is based on the T_{Mo} site.

Table 1. Binding Energy and Distance of Different Doping Positions

Modification Site	E_b (eV)	D (Å)
T_{Mo}	−2.25	2.611/2.613 (Pd−Te)
		3.108 (Pd−Mo)
T_H	−2.12	2.721/2.728 (Pd−Te)
		4.170/4.172 (Pd−Mo)
T_{Te}	−1.67	2.501 (Pd−Te)

An extensive analysis of the band structure (BS), total density of states (TDOS), and partial density of states (PDOS) is conducted to further explore the impact of Pd atom doping on the electronic properties of a $MoTe_2$ monolayer.[29] The analysis reveals that the bandgap of pristine $MoTe_2$ is 1.273 eV, a property that underscores its pronounced semiconducting behavior and indicates a substantial amount of energy is necessary for electrons to transition from the valence band to the conduction band. As depicted in Figure 2a, Pd atom doping reduces the bandgap of $MoTe_2$ to 1.209 eV, suggesting a potential increase in the conductivity of the $MoTe_2$ monolayer. Figure 2b highlights the modifications in the TDOS of the Pd-$MoTe_2$ monolayer. In comparison to pristine $MoTe_2$, the DOS of Pd-$MoTe_2$ shifts to the left, with a minor decrease in the peak. However, the overall shape of the TDOS closely resembles that of pristine $MoTe_2$, implying that Pd atom doping does not alter the original crystal structure of $MoTe_2$. The PDOS illustrated in Figure 2c indicates significant overlapping peaks between the Pd 4*d* and Mo 5*p* orbitals at −5−2 eV. This overlap indicates strong hybridization between the orbitals and the formation of Pd−Te chemical bonds.

The subsequent section of the paper analyzes changes in charge density and atomic orbital interactions by utilizing calculations of the charge density difference (CDD), DOS, TDOS, and BS of various adsorption systems.

3.2. Gas Adsorption Configurations of the Pd-$MoTe_2$ Monolayer. Figure 3 illustrates the geometric configurations of the SF_6 decomposition products. The H_2S molecule, as shown in Figure 3a, exhibits a V-shaped spatial structure, with a covalent bond angle (H−S−S) of 91.360° and an H−S bond length of 1.356 Å. Figure 3b reveals similar spatial structures for SO_2 and H_2S, characterized by a 119.900° bond angle and an S−O bond length of 1.481 Å. The S atom engages in unequal *sp*2 hybridization with two O atoms, in conjunction

https://doi.org/10.1021/acsomega.3c03569
ACS Omega 2023, 8, 28769−28777

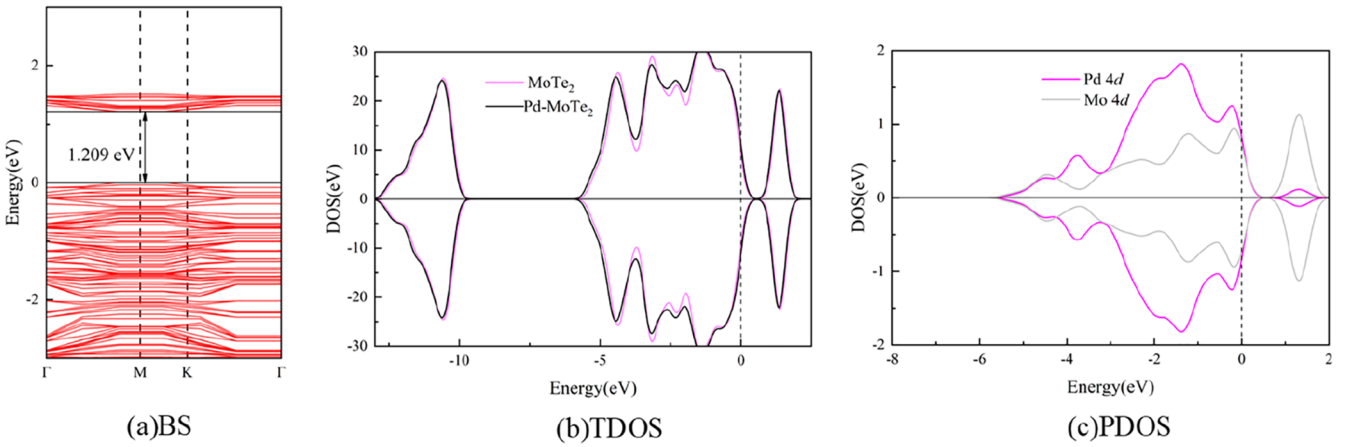

Figure 2. BS, TDOS, and PDOS of the Pd-$MoTe_2$ monolayer; the black arrows point to the VBM and CBM.

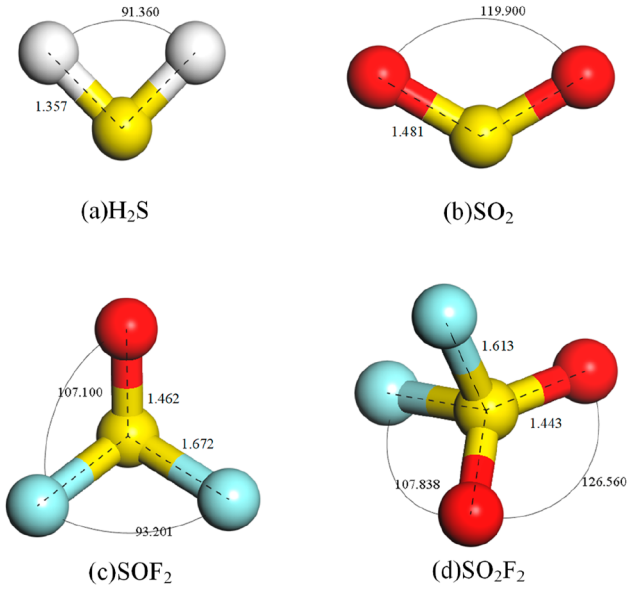

Figure 3. Structures of the SF_6 decomposition gas.

with a p orbital, thereby constituting a three-centered, four-electron Π bond system. As a result, the two S−O bonds emulate the properties of a double bond. SOF_2 possesses a planar triangular spatial configuration. As depicted in Figure 3c, the bond angles for F−S−O and F−S−F are 107.100° and 93.201°, respectively, with F−S and O−S bond lengths of 1.672 and 1.462 Å, respectively. The SO_2F_2 molecule, presented in Figure 3d, has an F−S−O bond angle of 107.838°, an F−S bond length of 1.613 Å, and an O−S bond length of 1.443 Å.

After studying the configuration of the gas molecule, we focus on analyzing the adsorption behavior of the Pd-$MoTe_2$ monolayer upon four gas molecules. The adsorption energy (E_{ad}) is defined as

$$E_{ad} = E_{Pd\text{-}MoTe_2/gas} - E_{Pd\text{-}MoTe_2} - E_{gas} \quad (2)$$

In Equation 2, $E_{Pd\text{-}MoTe_2/gas}$, $E_{Pd\text{-}MoTe_2}$, and E_{gas} denote the total energies of the gas adsorption system, a single layer of Pd-$MoTe_2$, and isolated gas molecules, respectively.

The charge transfer amount between the gas molecule and the crystal surface is calculated using the Mulliken charge method, given by

$$\Delta Q = Q_1 - Q_2 \quad (3)$$

In Equation 3, ΔQ denotes the quantity of charge transfer within the system with Q_1 and Q_2 signifying the charge states of the gas molecule after and before adsorption, respectively. A positive value for ΔQ indicates electron loss from the gas molecule and corresponding electron gain at the crystal surface during adsorption. Conversely, a negative ΔQ signifies that the gas molecule gains electrons, while the crystal surface loses electrons during the adsorption process.

We performed gas adsorption on the surface of the Pd-$MoTe_2$ monolayer, arranging each gas molecule in diverse configurations around the Pd atom, approximately 2.0 Å distant. Following the optimization of the structure, Equation 2 is used to calculate the adsorption energy of the system and select the MSC for further analysis. To better understand the charge transfer behaviors during the gas adsorption process, we calculate the CDD for each adsorption system. Figures 3 and 4 provide detailed illustrations. Additionally, Table 2 presents the adsorption parameters, including the adsorption energy (E_{ad}), charge transfer (Q_T), and bond length (D).

In the H_2S adsorption system, as illustrated in Figure 4, the H_2S gas molecule is slightly parallel to the Pd-$MoTe_2$. The adsorbed H_2S molecule forms a new chemical bond with Pd-$MoTe_2$, which presents a Pd−S bond length of 2.400 Å and an adsorption energy of −0.949 eV. As the adsorption energy is less than −0.800 eV, this suggests chemisorption. The molecular structure of H_2S remains largely unchanged postadsorption. According to Equation 3, the H_2S molecule becomes positively charged by 0.116 e after adsorption, which is consistent with the reducing nature of H_2S. The SO_2 adsorption system shares similarities with the H_2S adsorption system. The SO_2 molecule is positioned almost perpendicularly to the $MoTe_2$ surface, with the sulfur atom directed toward Pd and both S−O bonds extending into the vacuum region. The Pd−S bond length is determined to be 2.228 Å, slightly less than the combined covalent radii of Pd and S atoms (2.23 Å). This indicates a strong interaction between the Pd atom and the $MoTe_2$ surface, further affirming the stability of the doped structure. Furthermore, the Pd−Te bond length increases from 2.61 Å before the adsorption to 2.63, 2.66, and 2.69 Å,

https://doi.org/10.1021/acsomega.3c03569
ACS Omega 2023, 8, 28769−28777

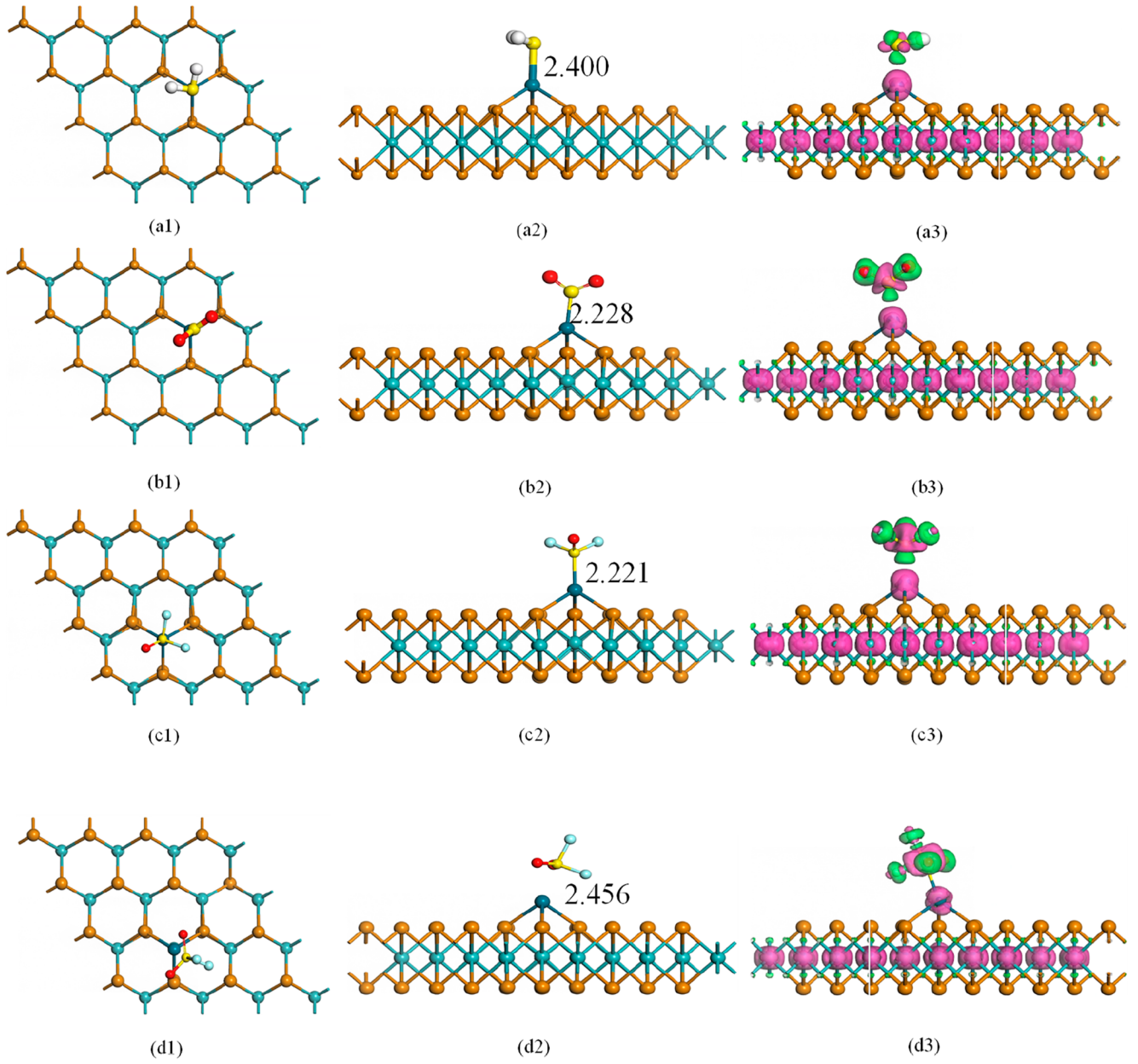

Figure 4. MSC (a1, a2, b1, b2, c1, c2, d1, d2) and CDD (a3, b3, c3, d3) for four gas adsorption system on the Pd-$MoTe_2$ monolayer (the green and rosy areas represent electron accumulation and depletion). (a1−a3) H_2S system, (b1−b3) SO_2 system, (c1−c3) SOF_2 system, and (d1−d3) SO_2F_2 system.

Table 2. Adsorption Energy (E_{ad}), Adsorption Distance (D), and Transferred Charge (Q) for the Best Adsorption Configuration of Four Gas Molecules on $MoTe_2$

Molecule	E_{ad} (eV)	Q_T (e)	D (Å)
H_2S	−0.949	0.116	2.400 (S−Pd)
SO_2	−1.268	−0.237	2.226 (S−Pd)
SOF_2	−1.063	−0.208	2.221 (S−Pd)
SO_2F_2	−0.272	−0.296	2.456 (S−Pd)

respectively, suggesting slight deformation induced by SO_2 adsorption. The adsorption energy amounts to −1.268 eV, which unequivocally suggests chemisorption. In accordance with Equation 3, SO_2 becomes negatively charged by 0.106 e after adsorption, while Pd gains 0.165 e of electrons, thereby concluding that the Pd-$MoTe_2$ loses 0.402 e of electrons during SO_2 adsorption. From the CDD in Figure 4b3, one can see that there is significant charge accumulation on the Pd−S bond and the Pd atom, which corroborates not only the orbital interaction during Pd−S bond formation but also the electron-donating properties of the Pd atoms.

In the SOF_2 adsorption system, it can be observed that the SOF_2 molecule tends to have the S atom facing the Pd-$MoTe_2$ surface while the other atoms are oriented upward for adsorption. The resulting Pd−S bond length is 2.221 Å, indicating its strong covalent bond property. The Pd−Te bond length extends to 2.66 Å, which is shorter than that in the SO_2 adsorption system, suggesting a relatively weaker interaction within the SOF_2 adsorption system. This inference is further confirmed by an adsorption energy of −1.06 eV. The CDD

https://doi.org/10.1021/acsomega.3c03569
ACS Omega 2023, 8, 28769−28777

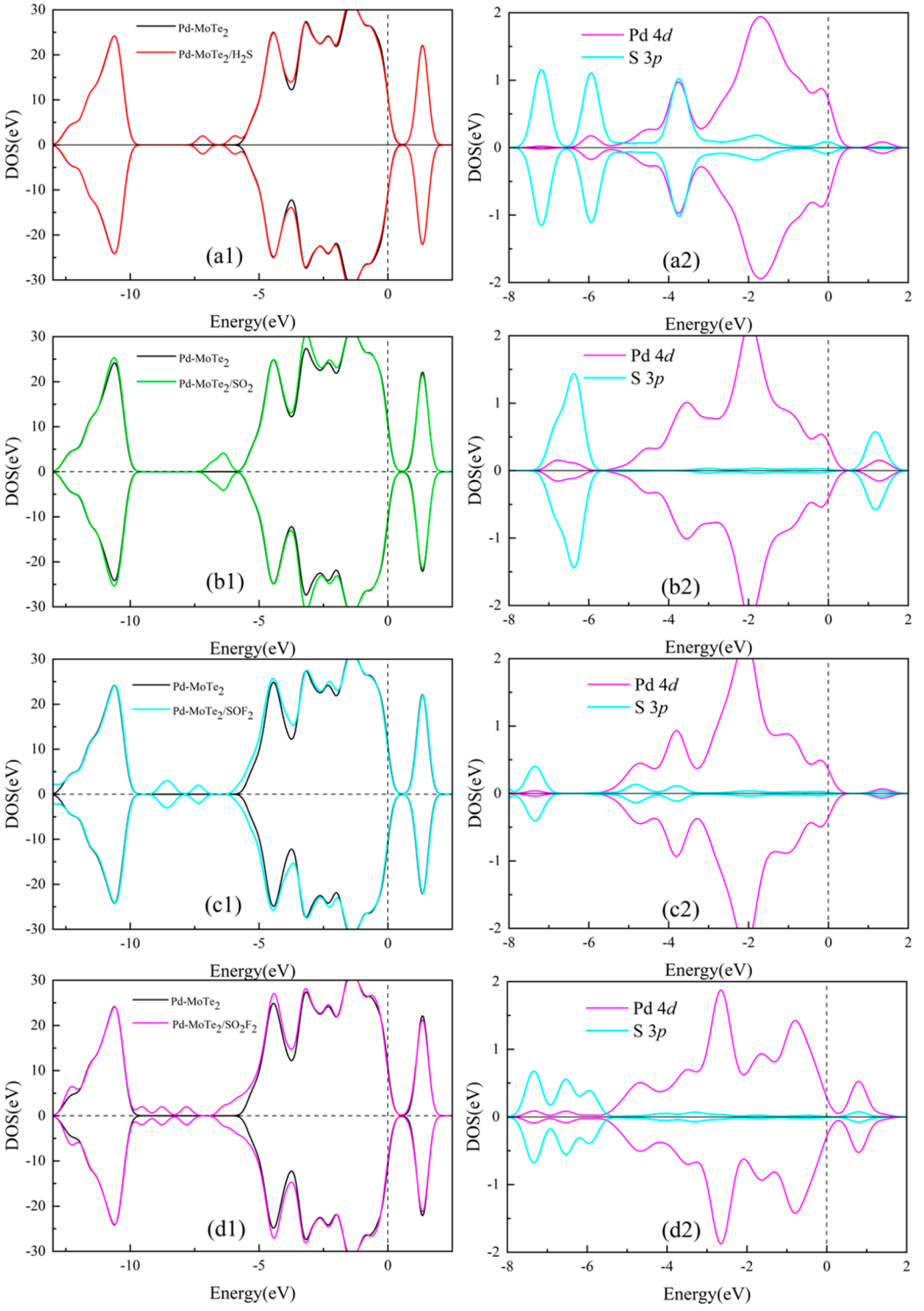

Figure 5. DOS (a1−d1) and PDOS (a2−d2) of H_2S (a1, a2), SO_2 (b1, b2), SOF_2 (c1, c2), and SO_2F_2 (d1, d2) systems. The dashed line is the Fermi level.

distribution reveals an accumulation of electrons around the Pd−S bond, which indicates a strong electron hybridization and orbital interaction at this location. Hirshfeld analysis suggests that the SOF_2 molecule loses 0.208 e of electrons, while the Pd atom acquires a positive charge of 0.154 e. Concerning the SO_2F_2 adsorption system, the SO_2F_2 molecule tends to adsorb via the S end. However, there is no substantial evidence to support the formation of a new bond between Pd-$MoTe_2$ and SO_2F_2. The Pd−S distance measures 2.45 Å, slightly longer than in the preceding three adsorption systems, and the SO_2F_2 molecule retains its geometric structure after interaction. These findings suggest that Pd-$MoTe_2$ exhibits relatively weak adsorption capabilities for SO_2F_2. The calculated adsorption energy of 0.27 eV implies physical adsorption. The CDD shows that electron accumulation is predominantly localized on the SO_2F_2 molecule, which is

https://doi.org/10.1021/acsomega.3c03569
ACS Omega 2023, 8, 28769−28777

consistent with the Q_T results based on the Hirshfeld analysis (−0.296 e).

3.3. Electronic Properties of the Pd-$MoTe_2$ Adsorption System. Figure 5 illustrates the DOS and PDOS for four adsorption systems, shedding light on the electronic behavior of Pd-$MoTe_2$ during gas adsorption.[30] It is observed that the densities of the spin-up and spin-down states maintain symmetry along the horizontal direction, indicating that the adsorbed systems remain nonmagnetic. In the H_2S adsorption system, despite the DOS remaining stable, the appearance of two new peaks at −6 eV and −7 eV is noted. Upon correlation with the PDOS, it is suggested that these new peaks primarily originate from the S 3*p* orbital. On the right side of the Fermi level, the distribution of TDOS in the Pd-$MoTe_2$ monolayer decreases upon adsorption of SO_2 and SOF_2 gases, suggesting a reduction in the number of occupied electrons and a significant chemical interaction taking place during the adsorption process. In the SO_2 adsorption system, the overall DOS shifts to the right, signifying that the doped Pd atom enhances both the chemical activity and the conductivity of the adsorption system. Moreover, there is a notable overlap between Pd 4*d* orbitals and S 3*p* orbitals at −6 and 2 eV, an indication of strong interactions between atomic orbitals and the formation of new bonds. In the SOF_2 adsorption system, the DOS exhibits new peaks at −7.5 eV, resulting from hybridization of the S 3*p* orbitals. Although the total DOS remains stable compared to the original, the peak height is slightly elevated. In the SO_2F_2 adsorption system, as evident from Figure 4d2, minimal hybridization occurs between Pd 4*d* and S 3*p* orbitals, demonstrating weak interaction during SO_2F_2 adsorption.

To further investigate the changes in the electrical conductivity of Pd-$MoTe_2$ after gas adsorption, we calculated and analyzed the band structures of four adsorption systems (Figure 6). In the band structure, the energy gap between the valence band and the conduction band is called the band gap, which represents the material's conductivity. A narrower band gap indicates easier electron transitions and higher conductivity. Upon observing Figure 6a−d, one can note the maximum valence band and minimum conduction band of four gas systems are located at the M point, indicating that the Pd-$MoTe_2$ monolayer maintains unaffected direct bandgap semiconductor properties during gas adsorption processes. On the other hand, in the SOF_2 adsorption system, compared to Pd-$MoTe_2$ in Figure 2, it can be observed that the bandgap slightly increases after SOF_2 gas is adsorbed, making it more difficult to excite electrons, thereby resulting in a decrease in overall conductivity. However, the systems of H_2S, SO_2, and SO_2F_2 exhibit divergent behavior, with novel states emerging near the Fermi level and significantly narrowing the bandgap. The bandgaps of Pd-$MoTe_2$ decrease upon adsorption of SO_2, SOF_2, and SO_2F_2 to 1.178, 1.152, and 1.069 eV, respectively. Interestingly, an impurity band state emerges in the middle of the band gap upon SO_2F_2 adsorption, indicating a significant alteration in the electronic property.

3.4. Work Function (WF) Analysis. WF denotes the least energy necessary to displace an electron from the interior to the exterior of a solid. For semiconductors, WF is represented by the difference between the vacuum and Fermi level, as depicted in Equation 4.[31]

$$\varphi = E_0 - E_F \tag{4}$$

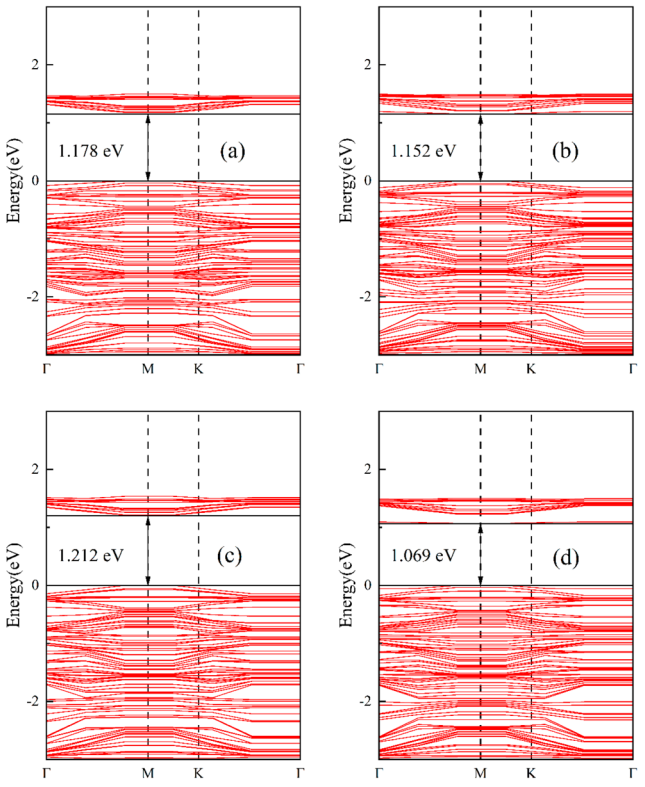

Figure 6. Band structures of H_2S (a), SO_2 (b), SOF_2 (c), and SO_2F_2 (d) systems. The dashed line is the Fermi level. The black arrows point to the VBM and CBM.

In Equation 4, φ represents the work function, E_0 represents the vacuum energy level, and E_F represents the Fermi level.

Figure 7 shows the WF of Pd-$MoTe_2$ and four other adsorption systems. The WF of the Pd-$MoTe_2$ adsorption

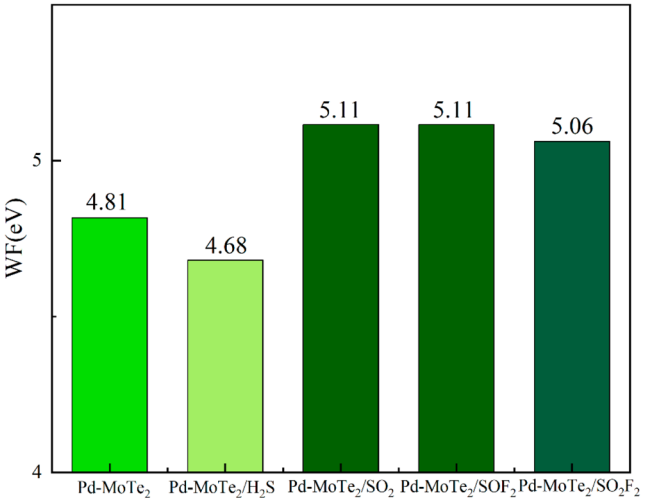

Figure 7. WF of the adsorption systems.

system is measured to be 4.81 eV. After the adsorption of H_2S, the WF decreases to 4.68 eV, suggesting a facilitated transfer of electrons from the Pd-$MoTe_2$ surface to the vacuum layer after H_2S adsorption. In contrast, the WF increases to 5.11, 5.11, and 5.06 eV, respectively, after the adsorption of SO_2, SOF_2, and SO_2F_2, with corresponding growth rates of 6.2%, 6.2%, and

https://doi.org/10.1021/acsomega.3c03569
ACS Omega 2023, 8, 28769−28777

5.2%. Thus, the Pd−$MoTe_2$ monolayer can be explored as a WF-based gas sensor for sensing SF_6 decomposition components, as well.

3.5. Recovery Property of the Pd-$MoTe_2$. Good reusability is important for gas sensors. It is worth noting that strong adsorption of certain molecules on Pd-$MoTe_2$ implies that the desorption of these gas molecules from Pd-$MoTe_2$ can be quite complex, and the device may require a longer recovery time. We understand that recovery time refers to the time required for gas desorption from the crystal surface, which is an important criterion for assessing the reusability of gas sensors. Transition state theory provides the relationship between recovery time (τ) and adsorption energy (E_a).[32,33]

$$\tau = \nu 0^{-1} e^{-E_a/kT} \quad (5)$$

where ν_0 is the attempt frequency, k is the Boltzmann's constant, and T is the temperature.[34] From Equation 5, it is apparent that temperature (T) and E_a are two important parameters that affect the value of τ.[35] When other parameters remain constant, lower E_a and higher temperature result in smaller τ values, respectively. As shown in Figure 8, it can be

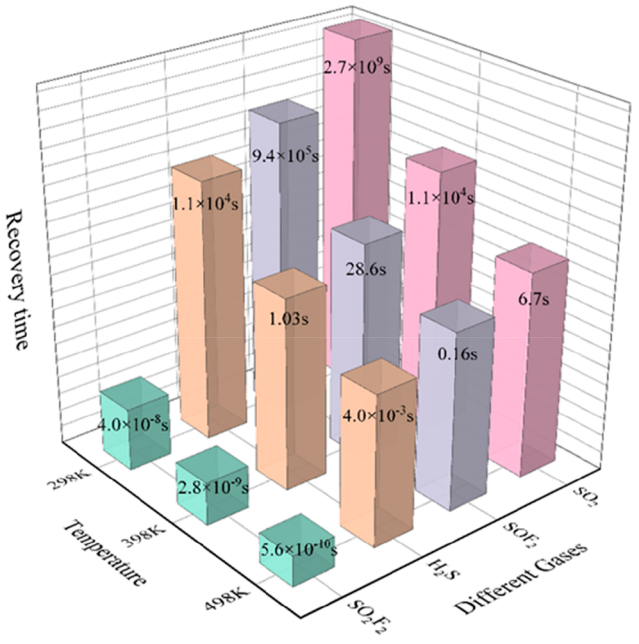

Figure 8. Recovery time of the Pd-$MoTe_2$ monolayer for gas desorption.

observed that the desorption of H_2S, SOF_2, and SO_2 from the surface of the Pd-$MoTe_2$ monolayer is relatively difficult at room temperature, but the recovery time decreases gradually with increasing temperature. On the other hand, the long recovery times for H_2S, SOF_2, and SO_2 at room temperature also confirm their strong chemical adsorption. We can see that, at 398 K, the recovery times for SOF_2 and H_2S systems are reduced to 28.6 and 1.03 s, respectively. At 498 K, the recovery time for the SO_2 system is 6.7 s. This means that the Pd-$MoTe_2$ monolayer can be reused as a gas sensing material for H_2S and SOF_2 detection at a temperature of 398 K and for SO_2 detection at a temperature of 498 K. However, due to weak binding with the Pd-$MoTe_2$ surface, SO_2F_2 exhibits a shorter recovery time. Therefore, the recovery of the Pd-$MoTe_2$ monolayer film at room temperature is not very ideal, but if the temperature of the sensor is increased, Pd-$MoTe_2$ will become a suitable sensor for detecting SF_6 decomposition gases.

4. CONCLUSIONS

This study establishes a Pd atom doping model on the Pd-$MoTe_2$ surface utilizing first-principles and further constructed adsorption models for four characteristic gases: SO_2F_2, SOF_2, SO_2, and H_2S, on the Pd-$MoTe_2$ surface. Throughout the adsorption process, a set of parameters are determined representing adsorption properties. The key conclusions at the mechanism level of the adsorption process are as follows:

(1) The calculation and comparison of the doping binding energy of Pd atoms in varying coordination on the $MoTe_2$ surface reveal that the Pd position above the Mo atom is the most stable doping state, exhibiting a binding energy of −2.25 eV and the bandgap of the Pd-$MoTe_2$ monolayer decreases to −1.209 eV.

(2) The transfer charges generated by the four gases H_2S, SO_2, SOF_2, and SO_2F_2 during the adsorption process are respectively 0.116, −0.237, −0.208, and −0.296 e. This is consistent with the process of electron dissipation and accumulation between gas molecules and Mo atoms in CDD.

(3) The most stable adsorption structures of H_2S, SO_2, SOF_2, and SO_2F_2 are determined in this study, and their respective adsorption energies, −0.949, −1.268, −1.063, and −0.272 eV, are calculated. The adsorption intensities are ranked as SOF_2 > SO_2 > H_2S > SO_2F_2. Notably, SO_2F_2 is physically adsorbed, whereas the others are chemically adsorbed, as further supported by the DOS analysis. BS analysis offers fundamental insights into the sensing mechanism of Pd-$MoTe_2$ as a potential resistive gas sensor.

(4) Compared to the Pd-$MoTe_2$ monolayer, the changing work function in the four gas systems indicates its potential as a gas sensor based on the work function to detect these SF_6 decomposition gases.

(5) The Pd-$MoTe_2$ monolayer film serves as a gas scavenger, capable of detecting SOF_2 and H_2S at 398 K, as well as SO_2 at 498 K, with recovery times of 28.6, 1.03, and 6.7 s, respectively. However, its recyclability at room temperature requires further exploration and improvement.

These results imply that the Pd-$MoTe_2$ monolayer demonstrates considerable potential as a chemical sensor to detect decomposition gases in SF_6 insulation equipment. Theoretically, Pd-$MoTe_2$ exhibits significant interactions with SOF_2 and SO_2, which can guide subsequent research on the experimental preparation of gas-sensitive sensors with selectivity and sensitivity.

AUTHOR INFORMATION

Corresponding Author

Shuangshuang Tian − *Hubei Engineering Research Center for Safety Monitoring of New Energy and Power Grid Equipment, Hubei University of Technology, Wuhan 430068, P. R. China; Guizhou Electric Power Test Research Institute, Guiyang 550002, China; Xiangyang Hubei University of Technology Industrial Research Institute, Xiangyang 441100, China*; Email: tianss@hbut.edu.cn

https://doi.org/10.1021/acsomega.3c03569
ACS Omega 2023, 8, 28769−28777

Authors

Chengjun Li − *School of Detroit Green Technology, Hubei University of Technology, Wuhan 430068, China;* orcid.org/0000-0002-5823-2280

Zengting Wang − *Hubei Engineering Research Center for Safety Monitoring of New Energy and Power Grid Equipment, Hubei University of Technology, Wuhan 430068, P. R. China*

Ying Zhang − *Guizhou Electric Power Test Research Institute, Guiyang 550002, China*

Complete contact information is available at: https://pubs.acs.org/10.1021/acsomega.3c03569

Notes

The authors declare no competing financial interest.

■ ACKNOWLEDGMENTS

This work is supported by the Key Research and Development Program of Hubei Province, China (No. 2020BAA022), and The China Postdoctoral Science Foundation (2021M690799).

■ REFERENCES

(1) Liu, H.C.; Wang, F.P.; Hu, K.L.; Li, T.; Yan, Y.Y.; Li, J. The Adsorption and Sensing Performances of Ir-modified MoS2Monolayer toward SF6 Decomposition Products: A DFT Study. *Nanomaterials* **2021**, *11*, 100.

(2) Hu, L.; Ottinger, D.; Bogle, S.; Montzka, S. A.; DeCola, P. L.; Dlugokencky, E.; Andrews, A.; Thoning, K.; Sweeney, C.; Dutton, G.; Aepli, L.; Crotwell, A. Declining, seasonal-varying emissions of sulfur hexafluoride from the United States. *Atmospheric Chemistry and Physics* **2023**, *23*, 1437−1448.

(3) Huan, W.; Xixiu, W.; Xiaotong, F.; Chao, L.; Xin, Y.; Shipu, W.; Hui, H.; Hongbin, L. Calculation and analysis the dynamic breakdown characteristic of SF6 discharge caused by GIS disconnector operation. *Phys. Scr.* **2023**, *98*, 025005.

(4) Xu, L. N.; Gui, Y. G.; Li, W. J.; Li, Q. M.; Chen, X. P. Gas-sensing properties of Ptn-doped WSe2 to SF6 decomposition products. *Journal of Industrial and Engineering Chemistry* **2021**, *97*, 452−459.

(5) Gui, Y. G.; Shi, J. Z.; Yang, P. A.; Li, T.; Tang, C.; Xu, L. N. Platinum modified MoS(2)monolayer for adsorption and gas sensing of SF(6)decomposition products: a DFT study. *High Voltage* **2020**, *5*, 454−462.

(6) Chen, B. S.; Li, H. K.; Zhao, X. M.; Gao, M.; Cheng, K.; Shao, X. P.; Wu, H. P.; Dong, L.; Yin, X. K. Trace photoacoustic SO2 gas sensor in SF6 utilizing a 266 nm UV laser and an acousto-optic power stabilizer. *Opt. Express* **2023**, *31*, 6974−6981.

(7) Bai, J. W.; Cong, P. J.; Zhang, H.; Sun, S. X.; Zhang, B. W.; Wang, Y.; Wang, L. Analysis of SF6 contact based on QPSO-SVR. *Energy Reports* **2023**, *9*, 425−433.

(8) Xiao, S.; Shi, S.; Li, Y.; Ye, F.; Li, Y.; Tian, S.; Tang, J.; Zhang, X. Review of decomposition characteristics of eco-friendly gas insulating medium for high-voltage gas-insulated equipment. *J. Phys. D: Appl. Phys.* **2021**, *54*, 373002.

(9) Franck, C. M.; Chachereau, A.; Pachin, J. SF6-Free Gas-Insulated Switchgear: Current Status and Future Trends. *Ieee Electrical Insulation Magazine* **2021**, *37*, 7−16.

(10) Li, C.; He, M.; Tian, S.; Yuan, J.; Wang, J.; Li, Y. Study on the Detection Characteristics and Response Mechanism of SnS2-Based Sensors for SO2 and SOF2. *Chemosensors* **2022**, *10*, 526.

(11) An, Y.; Yin, K.; Huang, T.; Hu, Y.; Ma, C.; Yang, M.; An, B.; Chen, D. Study on the Insulation Performance of SF6 Gas Under Different Environmental Factors. *Frontiers in Physics* **2022**, *10*, No. 820036.

(12) Jiang, T.; Zhang, W.; Zhang, T.; Yuan, H.; Bi, M.; Zhou, X. Adsorption and gas-sensing performances of C2H2, C2H4, CO, H2 in transformer oil on Pt-doped MoTe2 monolayer: A DFT study. *Physica E-Low-Dimensional Systems & Nanostructures* **2023**, *146*, 115568.

(13) Liu, Z.; Gui, Y.; Xu, L.; Chen, X. Adsorption and gas-sensing properties of Aun (n = 1−3) cluster doped MoTe2 for NH3, NO2, and SO2 gas molecules. *Surfaces and Interfaces* **2022**, *30*, 101883.

(14) Wu, D. Y.; Zhou, L. X.; Chen, C.; Liang, X. H. Adsorption Properties of Pt/N-doped Graphene for SF6 Decomposition Species. *Sens. Mater.* **2023**, *35*, 1413−1423.

(15) Xu, Z.L.; Cui, H.; Zhang, G.Z. Pd-Decorated WTe2Monolayer as a Favorable Sensing Material toward SF6 Decomposed Species: A DFT Study. *Acs Omega* **2023**, *8*, 4244.

(16) Cui, H.; Jia, P.F.; Peng, X.Y. Adsorption of SO2 and NO2 molecule on intrinsic and Pd-doped HfSe2 monolayer: A first-principles study. *Appl. Surf. Sci.* **2020**, *513*, 145863.

(17) Lin, L.; Feng, Z.; Dong, Z.; Hu, C.; Han, L.; Tao, H. DFT study on the adsorption of CO, NO2, SO2 and NH3 by Te vacancy and metal atom doped MoTe2 monolayers. *Physica E-Low-Dimensional Systems & Nanostructures* **2023**, *145*, 115489.

(18) Cao, W.; Zhao, Q.; Yang, L.; Cui, H. Enhanced NOx adsorption and sensing properties of MoTe2 monolayer by Ni-doping: A first-principles study. *Surfaces and Interfaces* **2021**, *26*, 101372.

(19) Zhou, R.; Wu, S.Q.; Cui, H.; Li, P.; Wu, T. First-principles investigation of Pt-doped MoTe2 for detecting characteristic air decomposition components in air insulation switchgear. *Computational and Theoretical Chemistry* **2022**, *1214*, 113796.

(20) Wang, M.; Zhou, Q.; Zeng, W. Theoretical study on adsorption of SF6 decomposition gas in GIS gas cell based on intrinsic and Ni-doped MoTe2 monolayer. *Appl. Surf. Sci.* **2022**, *591*, 153167.

(21) Wang, M.; Cheng, S.; Zeng, W.; Zhou, Q. Adsorption of toxic and harmful gas CO on TM (Ni, Pd, Pt) doped MoTe2 monolayer: A DFT study. *Surfaces and Interfaces* **2022**, *31*, 102111.

(22) Zhu, H.; Cui, H.; He, D.; Cui, Z.; Wang, X. Rh-doped MoTe2Monolayer as a Promising Candidate for Sensing and Scavenging SF6 Decomposed Species: a DFT Study. *Nanoscale Res. Lett.* **2020**, *15*, 129.

(23) Zhang, A.; Dong, Q.; Gui, Y.; Li, J.; Wan, F. Gas-Sensing Property of TM-MoTe2Monolayer towards SO2, SOF2, and HF Gases. *Molecules* **2022**, *27*, 3176.

(24) Wang, Z.; Zhang, G.; Liu, L.; Wu, Y.; Wang, J.; Xiao, S. Dissolved Gas Analysis in Transformer Oil Using Ni Catalyst Decorated PtSe2Monolayer: A DFT Study. *Chemosensors* **2022**, *10*, 292.

(25) Liu, L.; Zhang, G.; Wang, Z.; Yuan, J.; Tan, S.; Li, Y. Mo2C-Based Microfluidic Gas Sensor Detects SF6 Decomposition Components: A First-Principles Study. *Chemosensors* **2022**, *10*, 368.

(26) Cui, X.S.; Lu, Z.R.; Wang, Z.C.; Zeng, W.; Zhou, Q. Highly Sensitive SF6 Decomposition Byproducts Sensing Platform Based on CuO/ZnO Heterojunction Nanofibers. *Chemosensors* **2023**, *11*, 58.

(27) Zhang, X.X.; Wang, J.C.; Chen, D.C.; Liu, L. The adsorption performance of harmful gas on Cu doped WS2: A first-principle study. *Materials Today Communications* **2021**, *28*, 102488.

(28) Wang, J.; Zhang, X.; Liu, L.; Wang, Z. Adsorption of SF6 Decomposition Products by the S Vacancy Structure and Edge Structure of SnS2: A Density Functional Theory Study. *Acs Omega* **2021**, *6*, 28131−28139.

(29) Wu, D. Y.; Zhang, D. M.; Chen, C.; Zhou, L. X.; Liang, X. H. First-principles Study of SF6 Decomposed Gas Adsorption and Sensing on Pt and N Co-doped Graphene. *Sens. Mater.* **2023**, *35*, 1775−1783.

(30) Ju, L.; Tang, X.; Li, X.X.; Liu, B.D.; Qiao, X.Y.; Wang, Z.; Yin, H.B. NO2 Physical-to-Chemical Adsorption Transition on Janus WSSe Monolayers Realized by Defect Introduction. *Molecules* **2023**, *28*, 1644.

(31) Sun, H.; Tao, L.-Q.; Li, T.; Gao, X.; Wang, G.; Peng, Z.; Zhu, C.; Zou, S.; Gui, Y.; Xia, S.-Y.; Li, J. Sensing Characteristics of Toxic C4F7N Decomposition Products on Metallic-Nanoparticle Co-

Doped BN Monolayer: A First Principles Study. *Ieee Sensors Journal* **2021**, *21*, 13082−13089.
(32) Li, Z.J.; Teng, M.Z.; Yang, R.H.; Lin, F.Y.; Fu, Y.; Lin, W.Q.; Zheng, J.D.; Zhong, X.P.; Chen, X.D.; Yang, B.; Liao, Y.H. Sb-doped WO3 based QCM humidity sensor with self-recovery ability for real-time monitoring of respiration and wound. *Sensors and Actuators B-Chemical* **2022**, *361*, 131691.
(33) Zhang, Y.J.; Jiang, Y.D.; Duan, Z.H.; Wu, Y.W.; Zhao, Q.N.; Liu, B.H.; Huang, Q.; Yuan, Z.; Li, X.; Tai, H.L. Edge-enriched MoS2 nanosheets modified porous nanosheet-assembled hierarchical In2O3 microflowers for room temperature detection of NO2 with ultrahigh sensitivity and selectivity. *Journal of Hazardous Materials* **2022**, *434*, 128836.
(34) Zainal, M. A.; Chan, K. T.; Zainuddin, H.; Mohd Shah, N.; Raymond Ooi, C. H. First Principles Study of Toxic Gas Molecules Adsorption on Group IVA (C, Si, Ge) 2-Dimensional Materials. *Sains Malaysiana* **2023**, *52*, 625−639.
(35) Olegovich Bokov, D.; Jalil, A. T.; Alsultany, F. H.; Mahmoud, M. Z.; Suksatan, W.; Chupradit, S.; Qasim, M. T.; Delir Kheirollahi Nezhad, P. Ir-decorated gallium nitride nanotubes as a chemical sensor for recognition of mesalamine drug: a DFT study. *Mol. Simul.* **2022**, *48*, 438−447.

https://doi.org/10.1021/acsomega.3c03569
ACS Omega 2023, 8, 28769−28777